Flash infrared pulse time control of perovskite crystal nucleation and growth from solution

Sandy Sanchez[1,2], Xiao Hua[3], Antonio Guenzler[1], Esteban Bermudez[1], Dedy Septiadi[1], Michael Saliba[1], Ullrich Steiner[1*]*

1: Adolphe Merkle Institute, University of Fribourg, Chemin des Verdiers 4, 1700 Fribourg, Switzerland.

2: Laboratory of Photomolecular Science (LSPM), École Polytechnique Fédérale de Lausanne (EPFL), 1015 Lausanne, Switzerland.

3: Inorganic Chemistry Laboratory, University of Oxford, South Parks Road OX1 3QR, Oxford, UK.

Abstract

Flash infrared annealing (FIRA) of perovskite films allows the manufacture of compact layers for photovoltaic devices. This article addresses the use of long and short infrared pulses to control crystal nucleation and growth in perovskite films. By varying the FIRA parameters, it is possible to create high quality films of both fully inorganic and hybrid perovskites. This demonstrates the versatility of the FIRA protocol and establishes it as a fast synthesis process, which provides detailed control over the perovskite morphology and crystallinity.

Introduction

Solar cells based on hybrid perovskites (PSCs) with the ABX_3 structure, where A is Cs, MA or FA, B is Pb or Sn, and X is Cl, Br or I, have been optimized to yield power conversion efficiencies above 23%. The stability of these devices however still trail standard silicon solar cells[1,2-10]. Significant efforts were made to improve device durability by varying cation composition, architectures and interface passivation[11,7,4]. One approach towards stable PSCs is the replacement of the organic cation[12-15]. In particular, removing the volatile MA and adding instead inorganic Cs can improve the thermal device stability, which is significant for operational PSCs[16, 17]. Further

progress can be made by improving the synthesis methods and understanding the crystallization pathways in order to achieve a high perovskite film quality.

To this end, a control of the kinetics of the perovskite crystallization process is required to optimize the film quality. The recently reported flash infrared annealing (FIRA) method is a rapid thermal annealing technique, which allows to control several crystallization parameters, such as the in-plane size of the crystal domains[14, 18-20]. FIRA has been employed for the manufacture of highly crystalline organic-inorganic perovskite films and transparent inorganic conductive layers[14, 19]. FIRA has the potential scale-up PSC manufacture, combining large area film deposition with low thermal degradation[19].

To further expand the FIRA method, it is necessary to understand the physicochemical phenomena that take place during film crystallization. It is important, for example, to explore the pathways of crystal nucleation and growth and to identify intermediate phases that form during crystallization[21, 22]. While the overall process is similar in the commonly used "anti-solvent" (AS) method and FIRA, the difference lies in the speed of film formation, which in FIRA is faster than in the AS method (i.e. by using $MAPbI_3$)[23, 24]. As the solvents evaporate, supersaturation is eventually reached, initiating crystal growth from nuclei within the precursor liquid[25]. This kinetic process can be controlled through the FIRA illumination parameters.

This study discusses FIRA optimization for the creation of defect-tolerant perovskite thin films. During thin film formation, many aspects affect the crystallization and as a consequence the microstructure within the films, such as precursors, solvents, substrates and the annealing temperature. Solvent engineering and molecular additives, among others, have been developed to yield the desired morphologies in perovskite films[26-36]. Consequently, a variety of strategies to govern the crystal nucleation and growth of perovskite films were developed[28]. The hybrid lead halide perovskite precursor can form colloidal aggregates in solution causing complex nucleation and growth pathways[37, 38]. The diffusion of the molecules, solvent removal rate, and the crystal growth rate are critical in generating the kinetically trapped morphologies within the perovskite films. Therefore, in this work, we explore film formation during the annealing process by introducing a simple empirical framework, to develop an understanding of the role of the solvents, chemical precursors, and annealing time.

2. Crystal nucleation and growth as a function of pulse time

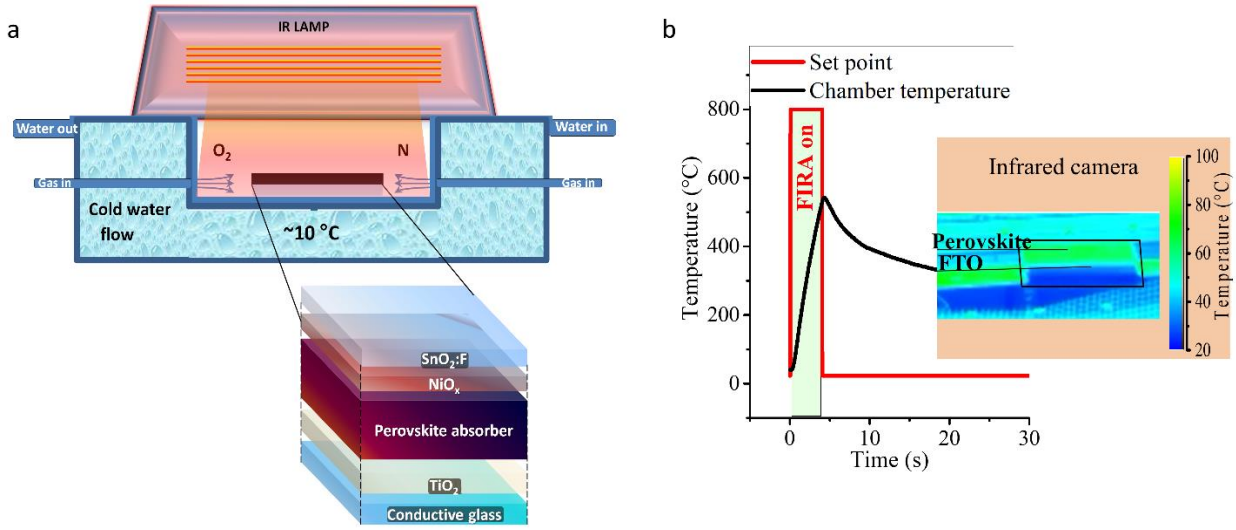

Figure 1. a) Schematic representation of the FIRA oven. b) Temperature profile in the oven during and after a 4-second infrared pulse. The inset shows the sample surface temperature after the pulse, measured by an infrared camera.

Figure 1**a** shows a schematic cross-section of the FIRA oven and a layered PSC architecture that is annealed inside the oven. This is described in the Supporting Information (SI), where FIRA-annealing was employed to synthesize NiO_x films on top of perovskite layers. The FIRA oven is composed of an array of near-infrared halogen lamps with an illumination power of 3000 kw/m[2,39]. A hollow aluminum body provides an effective water-cooling system. The use of aluminum is important because it reflects the IR light acting as a mirror to increase the light exposure of the sample[40]. Aluminum also has a high thermal conductivity, which enables the quick dissipation of heat[41]. Heat dissipation from the sample is further aided by blowing dry gas over the sample, removing heat and remaining solvent. In a typical experiment, a perovskite precursor solution is spin-cast onto an FTO substrate, which is then transferred into the FIRA oven. The FTO substrate absorbs the IR light and quickly heats up the precursor solution film[42]. Figure S1 shows the absorption spectra of FTO and ITO, which partially overlap with the spectral radiance of the halogen lamps. Figure 1**b** shows the temperature profile in the FIRA heating chamber. In only 4 seconds the chamber temperature reaches almost 600 °C, which is dissipated within 15 seconds after the light is off. The inset in Figure 1**b** shows a calibrated image of a sample taken by an

infrared camera, which shows that the maximum temperature of the perovskite film stays below 100 °C, minimizing the thermal degradation of the perovskite.

Once the solution is supersaturated through solvent evaporation, the nucleation rate is dominated by the critical nucleus size. Consequently, nucleation can be controlled by modulating the critical nucleus size, which is a function of the interfacial energy, keeping all other parameters fixed and assuming the simplest scenario of homogeneous nucleation[43]. The smaller the interfacial energy, the smaller is the critical nucleus size and the more likely nucleation becomes for a given supersaturation[44, 45]. During FIRA, crystal nucleation and growth can be controlled by three distinct parameters, the oven temperature, the pulse intensity and the pulse duration. Once nucleation has occurred, it is followed by the growth of a crystalline phase and for perovskite crystal formation, this can involve numerous intermediate phases[46]. The intense FIRA flash causes the rapid evaporation of the solvent and provides the driving force required for crystal nucleation and growth. Here molecular diffusion gradients play a fundamental role in how the system evolves far from thermodynamic equilibrium, through intermediate or metastable phases[47]. If sufficiently low, diffusion kinetically limits crystal growth.

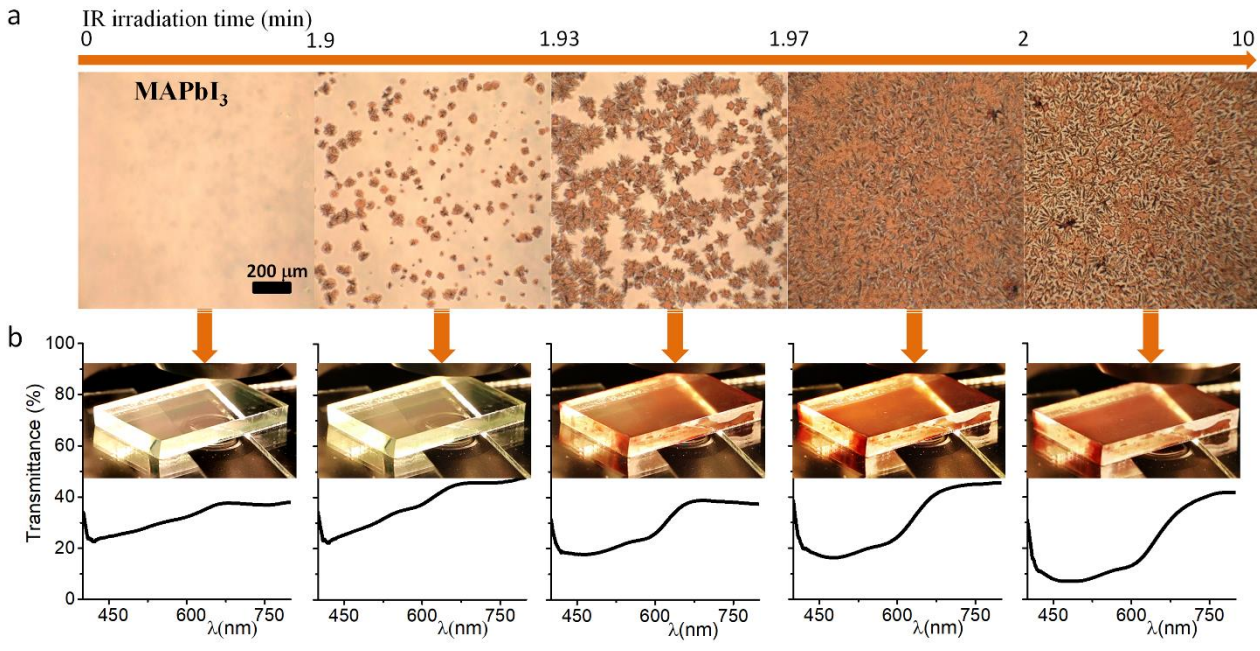

Figure 2. a) Optical transmittance micrographs of in-situ perovskite crystallization from solution during low intensity FIRA annealing (10% of the maximum intensity). b) Transmittance spectra and images of the samples.

To elucidate the perovskite crystallization dynamics, an in-situ experiment was performed using $MAPbI_3$ spin-coated solutions. Here the FIRA power was only 10% of its maximum intensity, to slow down and thus study the process in more detail. A video and transmittance spectra were recorded using a microscope in transmission illumination (Video 1 in the SI). Crystals start to grow from nucleation centers, going through intermediate phases along energetically favourable crystallographic directions in a dendritic growth, as shown Figure 2**a**[22, 48, 49]. The increase in crystal coverage can be seen by the change in color of the samples in Figure 2**b,** from yellow to brown, which is also observed in the transmittance spectra. Initially the transmittance varies almost linearly from 450 to 650 nm, which is characteristic for the liquid phase of the film. With increasing IR pulse time, a distinct absorption band spanning most of the visible spectral range develops. Note that the film does not reach its pure black phase in this experiment, indicating the substantial presence of unreacted material within the film.

2.1. Antisolvent and single-flash FIRA crystallization

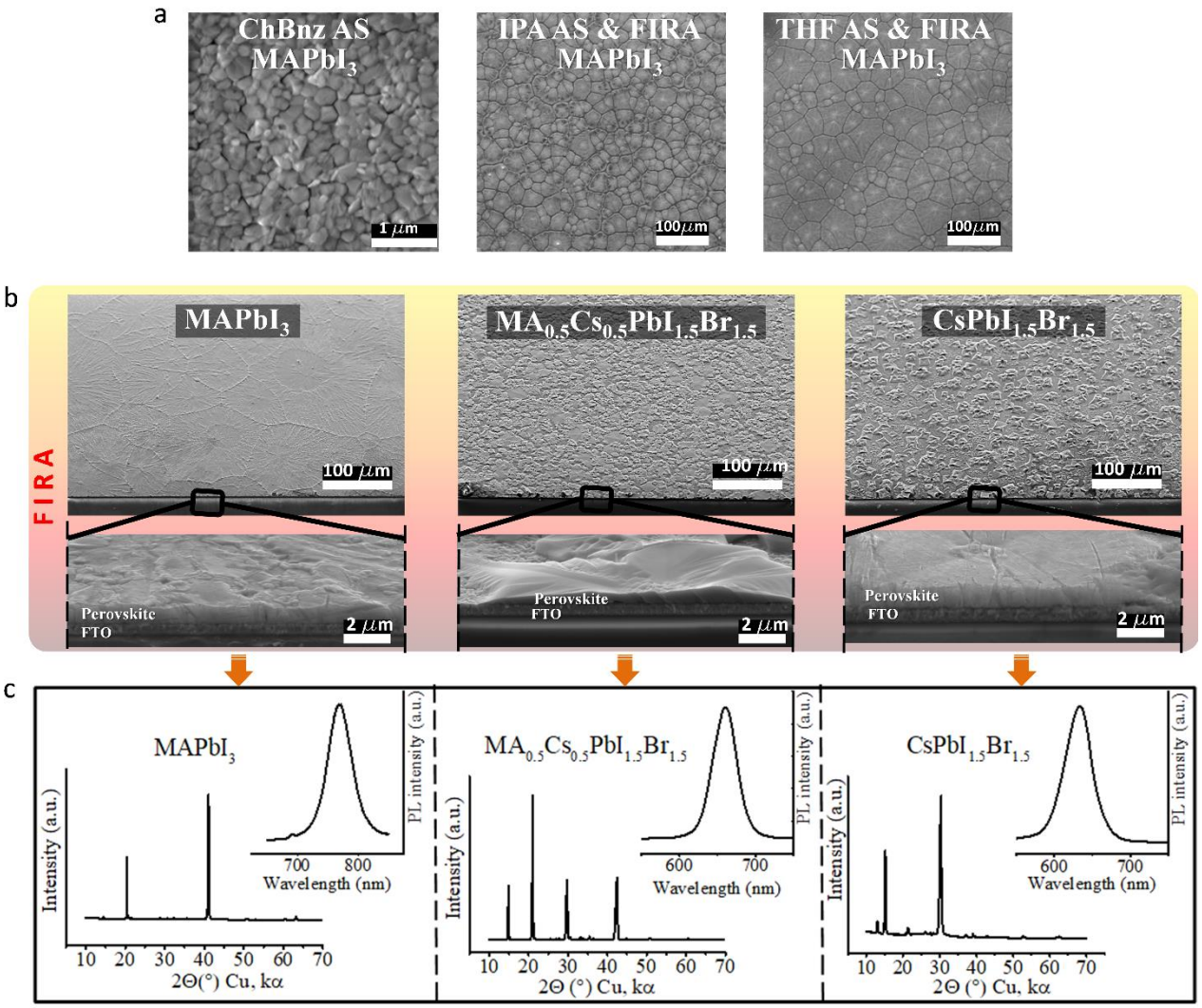

Figure 3. a) SEM images of films made by the AS method, using chlorobenzene (CB) as AS, and AS combined with FIRA annealing for two antisolvents, isopropyl alcohol (IPA) and tetrahydrofuran (THF). b) SEM images of FIRA annealed perovskite films of different cation compositions (the films have exposed to a 1.7 s IR flash), and c) corresponding XRD and PL emission spectra.

To examine the effects of the antisolvent on the grain size, several preparation parameters were fixed; a 1.7s FIRA illumination time, the number of seconds into the spin coating program at which antisolvent was deposited and the stoichiometric composition of the prepared perovskite solution. Using the AS method without FIRA creates a homogenous perovskite crystal morphology, as

shown Figure 3**a**. The addition of the antisolvent induces a high nucleation density by the rapid reduction in solubility of the perovskite precursors in the solvent mixture, followed by crystal growth of a new phase. The small crystal grain sizes arise from the high nucleation rate in the solvent mixture. FIRA on the other hand inputs a high amount of energy into the FTO layer in a single-flash to drive solvent evaporation, without degrading the perovskite film. In this way, supersaturation and crystal nucleation are achieved in a much more controllable fashion than AS. Note that the AS and FIRA methods have different crystal growth rates (and different thermal diffusion). Since crystal growth is faster in FIRA annealed films compared to the AS method, large crystalline domains are formed. The large crystalline domains of FIRA annealed films have an internal structure, unveiling the dendritic growth, as shown in the AFM image in Figure S2.

Figure 3**b** shows top-view and cross-sectional images of three perovskite chemical compositions annealed by a 1.7 second FIRA pulse. All films were cast from DMSO solution, varying the cation (MA, Cs) and halide (I, Br) compositions. The resulting morphologies shows how different perovskite compositions with mixed or single cations crystallize as a function of FIRA pulse time, corresponding to the overall energy deposited into the film. Differences in crystal morphologies are indicative of energy barriers that need to be overcome in the formation of a new phase[50]. If MA is replaced by Cs, the crystal tends to growth in a more homogeneous fashion from cluster nuclei and no dendritic growth is observed for the all inorganic composition[51, 52]. Furthermore, from the selected cross-sectional images in Figure 3**b**, different micro-shapes can be distinguished in the films, which arise from their differing cation compositions, keeping all other preparation parameters fixed.

Figure 3**c** shows the corresponding XRD patterns and the PL emission spectra for the three compositions. Interestingly, the diffraction pattern of tetragonal $MAPbI_3$ (space group *I*4/*mcm*) exhibits intense 2Θ peaks at 20° and 41° corresponding to (020) and (040) reflections, respectively, indicating a crystal growth with {010} planes parallel to the sample surface.[52-55] In contrast, the Bragg peaks for the AS $MAPbI_3$ thin film (Fig. S3) shows more resemblance to its powder pattern (by visual comparison), suggesting less textured characteristics for the AS-derived thin film. . These observations imply that the FIRA process can modify the crystal growth of perovskite through rapid quenching[53, 56, 57], hence different grain domain orientations in the corresponding thin films. In the case of mixed ion materials, based on the comparison of the relative peak intensities

of their XRD pattern between thin film (Fig. 3c) and powder (Fig. Sx) samples, $MA_{0.5}Cs_{0.5}PbBr_{1.5}I_{1.5}$ sample shows more pronounced difference revealing more textured characteristics comparing to the $CsPbBr_{1.5}I_{1.5}$ material. . The PL spectrum shows the corresponding emission for all the films, depending mainly on its halide combination, where the bromine addition blueshifts the spectra, as reported elsewhere[56, 59, 60].

2.2. Pulsed FIRA

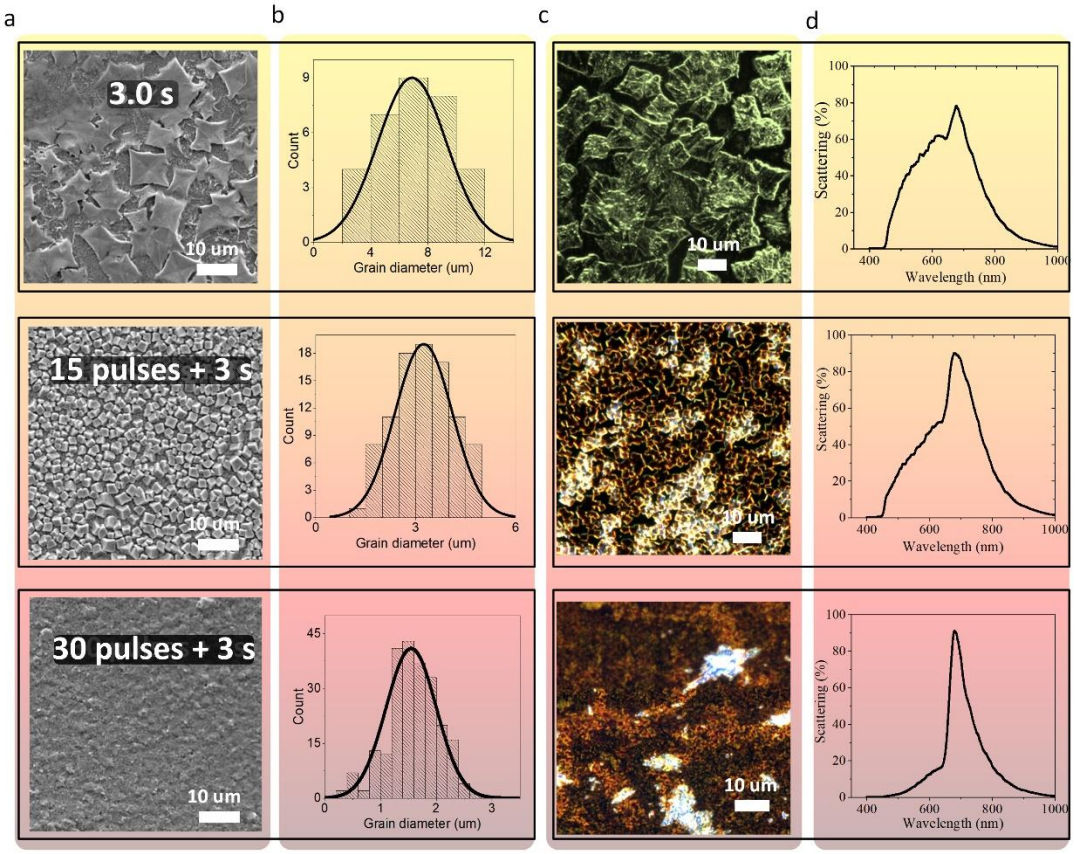

Figure 4. a) Top view SEM images of cesium lead halide films. b) Histogram of the crystal grain diameter; c) dark field-hyperspectral microscopy images; d) intensity of the scattered light spectra normalized to 100%.

Derived from FIRA perovskite synthesis, pulsed FIRA (*p*-FIRA) allows to drive crystal nucleation through a sequence of extremely short pulses, as reported previously[14]. So-called 20 ms "pulses" are followed by a long final "flash" of more than 1 s. *p*-FIRA results suggest that the perovskite nucleus density varies with the number of short pulses, adding new nuclei with each of a series of pulses. The long final annealing flash enables growth of already established nulcei. Figure 4**a** shows SEM images for 0, 15 and 30 pulses, exhibiting different grain diameters which are displayed in the histograms of Figure 4**b** for an inorganic perovskite. Starting from a single FIRA flash, the addition of up to 30 short pulses decreases the cuboid grain size from 10 μm to 1 μm. Figure 4**c** shows dark field-hyperspectral microscopy images and 4**d** plots the scattered light from the acquired image (randomly chosen points - see Experimental Methods for details). The scattered

light is higher from substrates that are only partially perovskite-covered, since the homogenous films scatter less light compared to those covered by crystal clusters. The scattered light decreases as the crystal size decreases, in particular the samples exposed to 30 shorts scatter only very little. These samples are covered by quasi-compact films due the high density of individual grains and the lack of gaps at their boundaries.

2.3. Warmed-pulsed FIRA

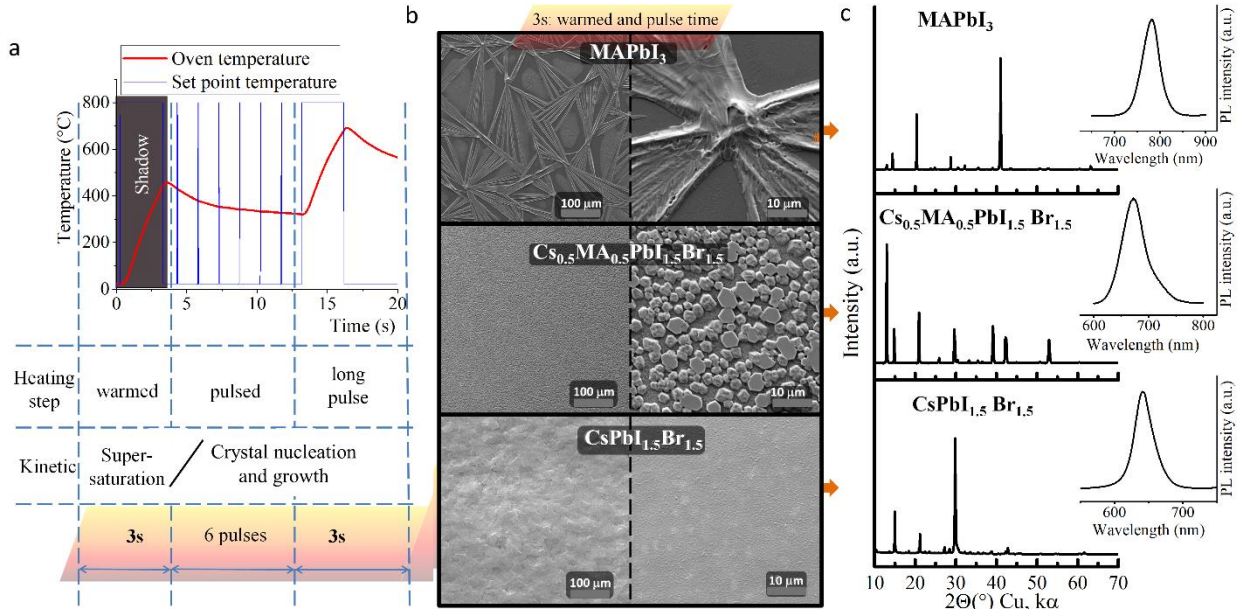

Figure 5. a) Temperature profile as a function of the time of the warmed-pulsed FIRA method and schematic of the processes. b) SEM top view images and c) XRD and PL emission spectra of three films of different perovskite compositions.

Warmed-pulsed FIRA (*wp*-FIRA), similar to *p*-FIRA makes use of short IR irradiation pulses (20 ms) to drive the crystal nucleation and growth of the thin film. The main feature of *wp*-FIRA is a reduction in the synthesis time to 15-20 seconds and it improves film compactness. Figure 5**a** shows the temperature as a function of time for *wp*-FIRA, consisting of three steps: 1) oven warming in the dark, 2) pulses and 3) a single last flash. Here, the liquid solution film is first warmed-up; the chamber is heated for 3 seconds by IR illumination, not exposing the sample to the light. The warm-up step is followed by six shorts pulses and a single flash of 3 seconds (the sample is placed into a shadow by a manual mechanism). Here, the introduction of the warming step convectively preheats the perovskite solution by generating a temperature gradient across the chamber. This initiates slow

solvent evaporation of the solution, which increases solution saturation, so that only a few subsequent IR-pulses are sufficient to nucleate perovskite seed crystals.

The *wp*-FIRA synthesis results in different film morphologies than *p*-FIRA as shown in Figure 5**b**. Using the standard $MAPbI_3$ perovskite, large needle shaped crystallites emerge from a nucleation center, which is characteristic for faceted or crystal spiky growth[61, 62]. Mixing in cesium cations and bromide anions, the *wp*-FIRA annealed morphology results in a hexagonal grain arrangement, which is different to single-flash FIRA annealing (Figure 3**b**) of the same perovskite. When entirely replacing MA by Cs, i.e. an all-inorganic perovskite composition, results in a smooth layer that is even more compact than the layer synthetized by *p*-FIRA. Figure S4 shows higher magnification SEM top views of inorganic perovskite films obtained by both methods. *wp*-FIRA annealing of this perovskite yields a very similar film in terms of crystallinity, texture (Fig. 5c) and morphology as single-flash FIRA and also exhibits similar photoluminescence emission, as shown Figure 3**c.**

FIRA methods	Synthesis time	Perovskite film morphology	
		Hybrid	Inorganic
Single-flash	~2 seconds	Compact film	Single island
Pulsed	~1 min	Non-compact film	Compact single cuboid
Warmed-pulsed	~15-20 seconds	Non-compact film	Compact film

Table 1. Characteristics of the three FIRA methods used for the perovskite film synthesis.

The synthesis method and perovskite crystallization are key for high performance devices. High quality compact, crystalline and defect-free films are a requirement for high performance PV devices. Table 1 summarizes the main features of the three FIRA methods described in this article. The single-flash FIRA method is rapid and works well in synthesizing hybrid perovskite films. Pulsed and warmed-pulsed FIRA have longer synthesis times but they are better suited to produce high-quality all-inorganic PSCs. In particular, *wp*-FIRA achieves the inorganic perovskite synthesis of a high film quality in a short processing time. This is further documented in in the SI, where *wp*-FIRA has been specifically chosen for the deposition of inorganic perovskite films.

3. Conclusion

The use of FIRA extends the processability of perovskite film synthesis from solution. It is highly controllable and thereby enables to tune the crystallinity, morphology and coverage of films for a wide range of perovskite compositions. In particular, this method is sufficiently flexible to adapt protocols to the different perovskite compositions, enabling good results in all of them. A knowledge of the underlying kinetic phenomena that are involved in the thin film formation opens up a parameter space that, on the one hand, allows the empirical optimization of the films, and on the other hand enables fundamental studies of crystallization and film formation processes. The IR pulse time is a key parameter to drive the crystallization of perovskite films through FIRA and to shape the suitable crystal morphology which can be used for device optimization. The derived knowledge will be useful to improve perovskite synthesis and film quality, which will result in better device performances. Compared to the AS method, the three FIRA techniques are suitable to scale-up PSC manufacture in terms of ease of implementation, reproducibility, synthesis time, and integration into an automatized device manufacture line.

4. Experimental Methods

Perovskite solar cell manufacture

Photovoltaic devices were fabricated on FTO coated glass (Pilkington NSG TEC™). The substrates were cleaned with Hellmanex soap, followed by 30 min sonication in a Hellmanex 2% water solution, 15 min sonication in IPA, and 5 min of oxygen plasma etching. Then, 10 nm thick TiO_2 compact layers were deposited onto the FTO by spray pyrolysis at 450 °C from a precursor solution of titanium diisopropoxide bis (acetylacetonate) in anhydrous ethanol and acetylacetonate. After spraying, the FTO substrates were left at 450 °C for 5 min before cooling to room temperature. Then, a mesoporous TiO_2 layer was deposited by spin-coating for 10 s at 4000 rpm with a ramp of 2000 rpm s^{-1}, using a 30-nm particle size TiO_2 paste (Dyesol 30 NR-D) diluted in ethanol to achieve 150-200 nm thick mesoporous layers. After spin-coating, the FTO substrates

were dried at 100 °C for 10 min, and the films were annealed on a programmable hotplate to crystallise TiO_2 at 450 °C for 30 min under dry air flow. Li-doping of the mesoporous TiO_2, as described elsewhere[63], was accomplished by spin coating a 0.1 M solution of bis(trifluoromethane)sulfonimide lithium salt (Li-TFSI) in acetonitrile at 3000 rpm for 10 s followed by another sintering step at 450 °C for 30 min. After cooling down to 150 °C, all the substrates were kept on the fume hood (with a relative humidity below to 38%) until the deposition of the perovskite films.

Perovskite solution preparation

The $MAPBI_3$ perovskite precursor solution contains MAI (1.2 M), PbI_2 1.2 M in anhydrous DMSO. The organic salts were purchased from Greatcell; the caesium and lead compounds from TCI. The hybrid perovskite precursor solutions were deposited from a precursor solution containing CH_5N_2I (1 M), PbI_2 (1.1 M), CH_3NH_3Br (0.2 M) and $PbBr_2$ (0.2 M) in anhydrous DMF: DMSO 4:1 (v:v). Note that this composition contains a lead excess as reported elsewhere[17]. Then CsI, dissolved as a 1.5 M stock solution in DMSO, was added to the mixed perovskite precursor to achieve the desired triple cation composition. The inorganic perovskite precursor was deposited from a solution containing CsI (1.2M), and to obtain the final stoichiometry of $CsPbI_xBr_{3-x}$ with x = 1.5, mixtures of PbI_2 (0.3 M), and $PbBr_2$ (0.9 M), respectively, were used.

FIRA Method

The films made by the FIRA method include the spin-coating of the perovskite solution in a single step at 4000 rpm for 10 s. The substrates were then IR irradiated for 1.7 s in the FIRA oven and were kept there for ten additional seconds before removal and cooling within several minutes. The samples made by pulsed-FIRA were exposed to 20 milliseconds pulses followed by a longer 2-second pulse. All the substrates were kept in the FIRA oven for 10 additional seconds before removal. The warmed-pulsed FIRA procedure was similar to pulsed-FIRA, but before applying 6 20 ms pulses, the IR lamps were switched on for a 3 seconds pulse while the sample was in the shadow of a manual shutter. FIRA processing was carried out in a fume hood.

AS & FIRA methods

The samples made by a combination of the two methods were spin coated in a single step at 4000 rpm for 15 s; 5 seconds before the end of spin-coating, 100 µl of IPA or THF (corresponding to the mentioned experiments in Figure 3**a**) was dropped onto the roating sample . Immediately after the spin-coating, the samples were IR irradiated for 1.7 s in the FIRA oven and were kept there for ten additional seconds before removal.

HTM deposition and contact back evaporation

Immediately after cooling the perovskite film, a spiro-OMeTAD (Merck) solution (70×10^{-3} M in chlorobenzene) was deposited by spin-coating at 4000 rpm for 20 s. Spiro-OMeTAD was doped with Li-TFSI (Sigma Aldrich), tris(2-(1H-pyrazol-1-yl)-4-*tert*-butylpyridine)-cobalt(III) tris(bis(trifluoromethylsulfonyl)imide) (FK209, Dynamo), and 4-*tert*-butylpyridine (TBP, Sigma-Aldrich). The molar ratio of the additives to spiro-OMeTAD was: 0.5, 0.03, and 3.3 for Li-TFSI, FK209, and TBP, respectively. The inorganic hole conducting layers were deposited as follows: a bis(methylcyclopentadienyl)nickel(II) (Merck) solution, 0.1 M in isopropyl alcohol, was deposited by spin-coating at 4000 rpm during 20 seconds. The nickel metalorganic layer was annealed from 10 to 40 min at 150 - 450°C in the flash infrared annealing oven. Finally, 1 nm of chromium was evaporated, followed by a 80 nm thick gold top-electrode, under high vacuum[64].

Experimental techniques

For photovoltaic measurements, a solar simulator from ABET Technologies (Model 11016 Sun 2000) with a xenon arc lamp was used and the solar cell response was recorded using a Metrohm PGSTAT302N Autolab. The intensity of the solar simulator was calibrated to 100 mW/cm^2 using a silicon reference cell from ReRa Solutions (KG5 filtered). *J-V*-curves were measured in reverse and forward bias at a scan rate of 10 mV/s. A shadow mask was used to define the device active area of 0.16 cm^2. Maximum power point tracking was used to perform stability experiments.

Material characterization

Scanning electron microscopy was carried out on a Tescan MIRA 3 LMH with a field emission source operated at an acceleration voltage of 10 kV. Powder X-ray diffraction was performed in transmission geometry with Cu target (λ = 1.5401Å) using an STOE STADI P diffractometer.

Optical transmission measurements were performed using a Zeiss Axio-Scope A1 Pol using a Zeiss EC Epiplan-Apochromat 10× objective and a xenon light source (Ocean Optics HPX-2000). For spectroscopic measurements, an optical fibre (QP230-2-XSR, 230 µm core) collected the transmitted light from the sample. The spectra were recorded by a spectrometer (Ocean Optics Maya2000 Pro), and a standard white diffuser was used as a reference. All spectra were obtained at room temperature in transmission. Photoluminescence spectra were obtained with Fluorolog 322 (Horiba Jobin Ybon Ltd) with a wavelength range of 600 nm to 850 nm by exciting at 460 nm. The samples were mounted at 60° and the emission was recorded at 90° from the incident beam path. AFM was carried out on a JPK Nanowizard II with a JPK Advanced SPM control station. AFM imaging was performed in tapping mode using rectangular Al-coated silicon cantilevers (NanoAndMore GmbH, k = 40 N m^{-1}, f = 300 kHz) with silicon tips (tip radius < 10 nm).

For enhanced dark field-hyperspectral imaging, the sample was placed on a sample holder and a drop of Immersol™ 518F immersion oil was added on top. The sample was illuminated by a Fiber-Lite® DC-950 lamp focused through a Cytoviva condenser and the scattered light was collected using a 100 × magnification lens (NA=0.8, Olympus BX-43). The scattered light was detected with a PCO Pixelfly camera system. In total, ten spectra from 10 randomly chosen spots were collected and the average spectrum of entire sample was calculated. The contact angles of advancing sessile drops of the probe liquids on the substrate were measured using a video-based optical contact angle measuring device (OCA 15pro, DataPhysics). All measurements were performed under air at room temperature with the SCA20 software (DataPhysics).

References

1. Q. Ma, S. Huang, S. Chen, M. Zhang, C. F. J. Lau, M. N. Lockrey, H. K. Mulmudi, Y. Shan, J. Yao, J. Zheng, X. Deng, K. Catchpole, M. A. Green and A. W. Y. Ho-Baillie, *The Journal of Physical Chemistry C*, 2017, **121**, 19642-19649.
2. M. Kulbak, S. Gupta, N. Kedem, I. Levine, T. Bendikov, G. Hodes and D. Cahen, *The Journal of Physical Chemistry Letters*, 2016, **7**, 167-172.
3. G. Abdelmageed, C. Mackeen, K. Hellier, L. Jewell, L. Seymour, M. Tingwald, F. Bridges, J. Z. Zhang and S. Carter, *Solar Energy Materials and Solar Cells*, 2018, **174**, 566-571.
4. R. E. Beal, D. J. Slotcavage, T. Leijtens, A. R. Bowring, R. A. Belisle, W. H. Nguyen, G. F. Burkhard, E. T. Hoke and M. D. McGehee, *The Journal of Physical Chemistry Letters*, 2016, **7**, 746-751.
5. T. A. Berhe, W.-N. Su, C.-H. Chen, C.-J. Pan, J.-H. Cheng, H.-M. Chen, M.-C. Tsai, L.-Y. Chen, A. A. Dubale and B.-J. Hwang, *Energy & Environmental Science*, 2016, **9**, 323-356.
6. B. Brunetti, C. Cavallo, A. Ciccioli, G. Gigli and A. Latini, *Scientific Reports*, 2016, **6**, 31896.
7. A. Calloni, A. Abate, G. Bussetti, G. Berti, R. Yivlialin, F. Ciccacci and L. Duò, *The Journal of Physical Chemistry C*, 2015, **119**, 21329-21335.
8. M. Saliba, M. Stolterfoht, C. M. Wolff, D. Neher and A. Abate, *Joule*, 2018, **2**, 1019-1024.
9. M. V. Khenkin, A. K. M, I. Visoly-Fisher, Y. Galagan, F. Di Giacomo, B. R. Patil, G. Sherafatipour, V. Turkovic, H.-G. Rubahn, M. Madsen, T. Merckx, G. Uytterhoeven, J. P. A. Bastos, T. Aernouts, F. Brunetti, M. Lira-Cantu and E. A. Katz, *Energy & Environmental Science*, 2018, **11**, 739-743.
10. M. Saliba, *Science*, 2018, **359**, 388-389.
11. G. Niu, X. Guo and L. Wang, *Journal of Materials Chemistry A*, 2015, **3**, 8970-8980.
12. A. Waleed, M. M. Tavakoli, L. Gu, S. Hussain, D. Zhang, S. Poddar, Z. Wang, R. Zhang and Z. Fan, *Nano Letters*, 2017, **17**, 4951-4957.
13. C. Liu, W. Li, C. Zhang, Y. Ma, J. Fan and Y. Mai, *Journal of the American Chemical Society*, 2018, DOI: 10.1021/jacs.7b13229.
14. S. Sanchez, N. Christoph, B. Grobety, N. Phung, U. Steiner, M. Saliba and A. Abate, *Advanced Energy Materials*, **0**, 1802060.
15. S.-H. Turren-Cruz, A. Hagfeldt and M. Saliba, *Science*, 2018, **362**, 449-453.
16. Y. G. Kim, T.-Y. Kim, J. H. Oh, K. S. Choi, Y.-J. Kim and S. Y. Kim, *Physical Chemistry Chemical Physics*, 2017, **19**, 6257-6263.
17. M. Saliba, T. Matsui, J.-Y. Seo, K. Domanski, J.-P. Correa-Baena, M. K. Nazeeruddin, S. M. Zakeeruddin, W. Tress, A. Abate, A. Hagfeldt and M. Gratzel, *Energy & Environmental Science*, 2016, **9**, 1989-1997.
18. S. Sanchez, X. Hua, N. Phung, U. Steiner and A. Abate, *Advanced Energy Materials*, DOI: 10.1002/aenm.201702915, 1702915-n/a.
19. S. Sanchez, X. Hua, N. Phung, U. Steiner and A. Abate, *Advanced Energy Materials*, 2018, **8**, 1702915.
20. S. Sánchez, M. Vallés-Pelarda, J.-A. Alberola-Borràs, R. Vidal, J. J. Jerónimo-Rendón, M. Saliba, P. P. Boix and I. Mora-Seró, *Materials Today*, 2019, DOI: https://doi.org/10.1016/j.mattod.2019.04.021.

21. P.-W. Liang, C.-Y. Liao, C.-C. Chueh, F. Zuo, S. T. Williams, X.-K. Xin, J. Lin and A. K.-Y. Jen, *Advanced Materials*, 2014, **26**, 3748-3754.
22. S. Sanchez, U. Steiner and X. Hua, *Chemistry of Materials*, 2019, DOI: 10.1021/acs.chemmater.9b00748.
23. Y. Zhou, M. Yang, O. S. Game, W. Wu, J. Kwun, M. A. Strauss, Y. Yan, J. Huang, K. Zhu and N. P. Padture, *ACS Applied Materials & Interfaces*, 2016, **8**, 2232-2237.
24. X. Zheng, B. Chen, C. Wu and S. Priya, *Nano Energy*, 2015, **17**, 269-278.
25. R. W. Schwartz, *Chemistry of Materials*, 1997, **9**, 2325-2340.
26. X. Fang, Y. Wu, Y. Lu, Y. Sun, S. Zhang, J. Zhang, W. Zhang, N. Yuan and J. Ding, *Journal of Materials Chemistry C*, 2017, **5**, 842-847.
27. Y. Wang, X. Guan, D. Li, H.-C. Cheng, X. Duan, Z. Lin and X. Duan, *Nano Research*, 2017, **10**, 1223-1233.
28. X. Zhou, Y. Zhang, W. Kong, M. Hu, L. Zhang, C. Liu, X. Li, C. Pan, G. Yu, C. Cheng and B. Xu, *Journal of Materials Chemistry A*, 2018, **6**, 3012-3021.
29. A. Dualeh, N. Tétreault, T. Moehl, P. Gao, M. K. Nazeeruddin and M. Grätzel, *Advanced Functional Materials*, 2014, **24**, 3250-3258.
30. C. Aranda, C. Cristobal, L. Shooshtari, C. Li, S. Huttner and A. Guerrero, *Sustainable Energy & Fuels*, 2017, DOI: 10.1039/C6SE00077K.
31. B. Xia, Z. Wu, H. Dong, J. Xi, W. Wu, T. Lei, K. Xi, F. Yuan, B. Jiao, L. Xiao, Q. Gong and X. Hou, *Journal of Materials Chemistry A*, 2016, **4**, 6295-6303.
32. K. Sangwal, *Progress in Crystal Growth and Characterization of Materials*, 1998, **36**, 163-248.
33. G. E. Eperon, V. M. Burlakov, P. Docampo, A. Goriely and H. J. Snaith, *Advanced Functional Materials*, 2014, **24**, 151-157.
34. D. Bi, J. Luo, F. Zhang, A. Magrez, E. N. Athanasopoulou, A. Hagfeldt and M. Grätzel, *ChemSusChem*, 2017, **10**, 1624-1630.
35. H. Tsai, W. Nie, P. Cheruku, N. H. Mack, P. Xu, G. Gupta, A. D. Mohite and H.-L. Wang, *Chemistry of Materials*, 2015, **27**, 5570-5576.
36. J.-P. Correa-Baena, M. Anaya, G. Lozano, W. Tress, K. Domanski, M. Saliba, T. Matsui, T. J. Jacobsson, M. E. Calvo, A. Abate, M. Grätzel, H. Míguez and A. Hagfeldt, *Advanced Materials*, 2016, **28**, 5031-5037.
37. K. Yan, M. Long, T. Zhang, Z. Wei, H. Chen, S. Yang and J. Xu, *Journal of the American Chemical Society*, 2015, **137**, 4460-4468.
38. Q. Hu, L. Zhao, J. Wu, K. Gao, D. Luo, Y. Jiang, Z. Zhang, C. Zhu, E. Schaible, A. Hexemer, C. Wang, Y. Liu, W. Zhang, M. Grätzel, F. Liu, T. P. Russell, R. Zhu and Q. Gong, 2017, **8**, 15688.
39. F. NINOMARU and I. H. , *JST Material*, 1985, **69**, 5.
40. D. Y. Smith, E. Shiles and M. Inokuti, in *Handbook of Optical Constants of Solids*, ed. E. D. Palik, Academic Press, Burlington, 1997, DOI: https://doi.org/10.1016/B978-012544415-6.50016-9, pp. 369-406.
41. R. E. B. Makinson, *Mathematical Proceedings of the Cambridge Philosophical Society*, 2008, **34**, 474-497.
42. L. Yue, B. Yan, M. Attridge and Z. Wang, *Solar Energy*, 2016, **124**, 143-152.
43. J. J. De Yoreo and P. G. Vekilov, *Reviews in Mineralogy and Geochemistry*, 2003, **54**, 57-93.
44. Y. Wang, Y. Shi, G. Xin, J. Lian and J. Shi, *Crystal Growth & Design*, 2015, **15**, 4741-4749.

45. T. Salim, S. Sun, Y. Abe, A. Krishna, A. C. Grimsdale and Y. M. Lam, *Journal of Materials Chemistry A*, 2015, **3**, 8943-8969.
46. M. Xiao, F. Huang, W. Huang, Y. Dkhissi, Y. Zhu, J. Etheridge, A. Gray-Weale, U. Bach, Y.-B. Cheng and L. Spiccia, *Angewandte Chemie International Edition*, 2014, **53**, 9898-9903.
47. K. A. Jackson, 2004.
48. S. C. Watthage, Z. Song, G. K. Liyanage, A. B. Phillips and M. J. Heben, 2016.
49. Z. Yao, T. W. Jones, M. Grigore, N. W. Duffy, K. F. Anderson, R. B. Dunbar, K. Feron, F. Hao, H. Lin and G. J. Wilson, *ACS Applied Materials & Interfaces*, 2018, **10**, 14673-14683.
50. B. J. Foley, J. Girard, B. A. Sorenson, A. Z. Chen, J. Scott Niezgoda, M. R. Alpert, A. F. Harper, D.-M. Smilgies, P. Clancy, W. A. Saidi and J. J. Choi, *Journal of Materials Chemistry A*, 2017, **5**, 113-123.
51. D. P. McMeekin, Z. Wang, W. Rehman, F. Pulvirenti, J. B. Patel, N. K. Noel, M. B. Johnston, S. R. Marder, L. M. Herz and H. J. Snaith, *Advanced Materials*, 2017, **29**, 1607039.
52. L. Protesescu, S. Yakunin, M. I. Bodnarchuk, F. Krieg, R. Caputo, C. H. Hendon, R. X. Yang, A. Walsh and M. V. Kovalenko, *Nano Letters*, 2015, **15**, 3692-3696.
53. P. S. Whitfield, N. Herron, W. E. Guise, K. Page, Y. Q. Cheng, I. Milas and M. K. Crawford, *Scientific Reports*, 2016, **6**, 35685.
54. F. Brivio, A. B. Walker and A. Walsh, *APL Materials*, 2013, **1**, 042111.
55. W. A. Saidi and J. J. Choi, *The Journal of Chemical Physics*, 2016, **145**, 144702.
56. S. Du, L. Jing, X. Cheng, Y. Yuan, J. Ding, T. Zhou, X. Zhan and H. Cui, *The Journal of Physical Chemistry Letters*, 2018, **9**, 5833-5839.
57. C. Quarti, E. Mosconi, J. M. Ball, V. D'Innocenzo, C. Tao, S. Pathak, H. J. Snaith, A. Petrozza and F. De Angelis, *Energy & Environmental Science*, 2016, **9**, 155-163.
58. Y. Huang, W.-J. Yin and Y. He, *The Journal of Physical Chemistry C*, 2018, **122**, 1345-1350.
59. I. L. Braly, D. W. deQuilettes, L. M. Pazos-Outón, S. Burke, M. E. Ziffer, D. S. Ginger and H. W. Hillhouse, *Nature Photonics*, 2018, **12**, 355-361.
60. G. Li, J. Huang, H. Zhu, Y. Li, J.-X. Tang and Y. Jiang, *Chemistry of Materials*, 2018, **30**, 6099-6107.
61. C. E. Miller, *Journal of Crystal Growth*, 1977, **42**, 357-363.
62. M. A. Lovette and M. F. Doherty, *Crystal Growth & Design*, 2013, **13**, 3341-3352.
63. *Organic Process Research & Development*, 2002, **6**, 201-202.
64. K. Domanski, J.-P. Correa-Baena, N. Mine, M. K. Nazeeruddin, A. Abate, M. Saliba, W. Tress, A. Hagfeldt and M. Grätzel, *ACS Nano*, 2016, **10**, 6306-6314.